Cellulose (2023) 30:9027–9046
https://doi.org/10.1007/s10570-023-05416-0

ORIGINAL RESEARCH

Dielectric and dynamic antibacterial investigations of organic–inorganic conductive membranes based on oxidized cellulose with BNKT nanoceramics

Ahmed I. Ali · Bahaa A. Hemdan · A. M. Mansour · Ali B. Abou Hammad · Samir Kamel · Amany M. El Nahrawy

Received: 26 August 2022 / Accepted: 19 July 2023 / Published online: 4 August 2023

Abstract The development of eco-friendly materials for advanced applications is highly demanded. The current study focuses on the preparation of conductive membranes based on tricarboxylic cellulose (TCC) loaded with cubic bismuth sodium titanate (BNKT) nanoceramics. FTIR, SEM, and EDX analyses confirm the presence of loaded BNKT on the membranes. The electrical response of the cellulose/xBNKT (x = 5, 10, 15, and 20% wt/wt) membrane is investigated using impedance spectroscopy. The real part (Z′) and the imaginary part (Z″) of the complex impedance are studied as a function of frequency (4Hz ~ 8MHz) and temperature (20 ~ 160 °C) for the different compositions. Impedance and modulus studies reveal a Debye-type relaxation phenomenon. The dielectric studies manifest promising dielectric properties. The bactericidal performance of all nanomembranes is evaluated. The nanomembrane with 20% BNKT (C20) exhibits bactericidal activity against Gram-negative and Gram-positive bacteria, with 6 log CFU reductions observed after an exposure time of 180 min. Treatment with the C20 nanomembrane shows the highest amounts of protein efflux. The results indicate that the C20 nanomembrane layer eradicated all bacterial cells. The findings suggest that the C20 nanomembrane is recommended as an intelligent and innovative antibacterial nano-system for bio-applications.

Keywords BNKT · Tricarboxy cellulose · Complex impedance · Electrical modules · Cole–Cole plot · Cytotoxicity · Antimicrobial activities · Food packaging

A. I. Ali
Basic Science Department, Faculty of Technology and Education, Helwan University, Saray–El Qoupa, El Sawah Street, Cairo 11281, Egypt

A. I. Ali
Nano-technology Research Center (NTRC), The British University in Egypt (BUE), El Sherouk City, Cairo 11837, Egypt

B. A. Hemdan
Water Pollution Research Department, Environmental and Climate Change Research Institute, National Research Centre, 33 El-Bohouth St., Dokki, Giza 12622, Egypt

A. M. Mansour · A. B. Abou Hammad (✉) · A. M. El Nahrawy
Solid State Physics Department, Physics Research Institute, National Research Centre, 33 El-Bohouth St., Dokki, Giza 12622, Egypt
e-mail: abohmad2@yahoo.com

S. Kamel
Cellulose and Paper Department, National Research Centre, Dokki, Giza 12622, Egypt

Introduction

Rapid energy storage technology requires affordable, flexible, and eco-friendly materials. Electrostatic capacitors have garnered significant attention

due to their ability to store energy through dielectric polarization (Dang et al. 2012; Prateek et al. 2016; Goodman et al. 2022). Electrostatic capacitors possess superior characteristics, including high intrinsic power density, efficient charge and discharge, exceptional stability, long lifespan, and a wide range of applications in electric power systems, pulsed electronics, and electric and hybrid vehicles (Yang et al. 2018). The development of power electronics entails increasing the energy density of the dielectric capacitors (Goodman et al. 2022).

Metal oxides such as $BaTiO_3$ and $SrTiO_3$ are traditional dielectrics with Strong polarization capabilities but lack flexibility and have low breakdown strength. Polymeric materials offer an alternative to metal oxides due to their exceptional flexibility, superior dielectric strength, and potential for manufacturing (Palneedi et al. 2018). However, the drawback of polymeric materials is their low dielectric permittivity, which limits their energy density. Therefore, the challenge lies in fabricating dielectric hybrid nanocomposite materials that combine higher dielectric constants, outstanding flexibility, dielectric strength, and energy density by creating polymeric-metal oxide composites.

Polymers have been chemically modified to develop new biomaterials with unique physicochemical properties. Cellulose is an inexhaustible and widespread biopolymer with unique properties. It is naturally abundant, renewable, biodegradable, biocompatible, hydrophilic, dimensionally stable, easily chemically modified, has a low thermal expansion coefficient, and exhibits a high Young's modulus. Moreover, it consists of repeated glucose units as the main constituent of the plant cell wall (Kamel and Khattab 2021).

Cellulosic composites have recently become the subject of extensive research in energy harvesting and storage. Flexible dielectric composites have been fabricated based on the mixture between cellulose and various inorganic nanofillers such as $BaTiO_3$, MoS_2, AgBr, and AgCl. Generally, cellulose and its derivatives have been employed for different applications, such as coatings, pharmaceutical industries, foodstuffs, immobilization of proteins and antibodies, sensors, laminates, textiles, optical membranes, and catalysis. Furthermore, biocompatible hydrogels based on aldehyde-functionalized cellulose and chitosan offer the potential control of drug release (Lal and Mhaske 2018; Yin et al. 2020; Song et al. 2022).

Various forms of antimicrobial active packaging include immediate embedding of bioactive molecules into a biopolymer matrix, utilization of polymers' intrinsic antimicrobial properties, deposition onto packaging surfaces, or immobilization in bags and patches through ionic or covalent couplings (Vilela et al. 2018; Sharma et al. 2020).

Effective antimicrobial molecules derived from natural resources (e.g., chitosan, nisin, lysozyme, plant essential oils, tea polyphenols, and others), synthetic organic antimicrobial agents (such as chloramphenicol and nalidixic acid), and inorganic antibacterial agents (some of the oxidized nanoparticles), are employed in bio-sensors (Ju et al. 2019). Many inorganic and metal nanoparticles are utilized in energy storage systems and food packaging products. However, achieving biocompatibility between nanostructures and polymeric composites remains a significant challenge in nanocomposite development (El Nahrawy et al. 2022).

Cellulose, with its multiple OH groups per monomer unit, can be functionalized by oxidation using various oxidizing agents, such as periodates, TEMPO/sodium bromide, hydrogen peroxide, chlorine dioxide, and peracetic acid. Recently, the TEMPO/sodium bromide system has been widely used for converting primary hydroxyl groups (C6) to carboxylic groups (–COOH), thereby modifying the surface of cellulose. Periodate oxidation of cellulose cleaves the C2–C3 bonds of the glucopyranose ring, resulting in the formation of 2,3-dialdehyde cellulose (Hasanin et al. 2021).

Water-soluble carboxyl cellulose was prepared by Sergiu et al. using a combination of two nitroxyl-mediated reactions and periodate oxidation in a one-shot response (Coseri et al. 2015). Tricarboxylic cellulose was synthesized in three steps involving the reaction of cellulose with N_2O_4, $NaIO_4$, and $HClO_2$. It is important to note that these reactions using N_2O_4, $NaIO_4$, and chloroform are conducted with toxic and explosive reagents (Takaichi et al. 2014).

Therefore, the main objective of this research is to develop intelligent conductive nanomembranes suitable for various applications by loading BNKT nanoceramics onto tricarboxylic cellulose (TCC). Advanced BNKT nanoceramics, prepared using

conventional powder processing, are loaded into TCC, forming noncovalent bonds within the TCC matrix.

Various characterizations were performed to provide better investigations of the nanomembranes BNKT/TCC, which clarify their advantageous structural, thermal, and dielectric properties for various applications. Additionally, antimicrobial activity and its statistical analysis were investigated to confirm their suitability and bioactivity. These characterizations aimed to enhance our understanding of the advanced organic–inorganic nanocomposites.

Materials and methods

Materials

Bleached Bagasse pulp was provided by Quena-Company of Paper Industry, Egypt. Titanium Oxide TiO_2, Potassium oxide K_2O, Bismuth nitrate $Bi(NO_3)_2$, and Sodium carbonate $NaCO_3$ were purchased from Aldrich, U.S.A. Sodium meta periodate ($NaIO_4$), 2,2,6,6-tetramethylpiperidine-1-oxyl (TEMPO), and sodium bromide (NaBr) were purchased from Sigma-Aldrich. A crosslinker polyamide-amine-epichlorohydrin (PAE) with approximately 33% solid content (w/w) was bought from Solines, Wilmington, DE, USA, and diluted to 1 wt% with distilled water before addition.

Sample preparation

Metal oxide preparation

The conventional powder processing unit was used to prepare the bulk ceramic material $Bi_{0.5}Na_{0.25}K_{0.25}TiO_3$ (BNKT). The powders were thoroughly mixed in an ethanol medium with the zirconia's balls by stirring them in a high-speed turbine at 5000 rpm for 24 h. The slurry was then dried at 120 °C. The mixtures were ground into powder, lightly crushed in the agate mortar, and finely sieved using a 100-µm mesh screen. The resulting nanopowder was fired at 1150 °C for 6 h.

Oxidation of the cellulose onto tricarboxy cellulose (TCC)

The cellulose was oxidized to tricarboxy cellulose using TEMPO/sodium bromide, followed by sodium periodate and sodium chlorite (Abou-Zeid et al. 2018). In this process, 50 ml of 10% sodium hypochlorite was added to a mixture of TEMPO and sodium bromide (0.5 and 8 mmol, respectively), along with 5 g of cellulose dispersed in 500 ml of water. The pH was adjusted to 10 and stirred overnight. Subsequently, the solution was neutralized, centrifuged at 7000 rpm, and rinsed with water for a week. The TEMPO- oxidized cellulose was oxidized by adding sodium periodate to the reaction ampule and covered with aluminum foil to prevent photo-induced decomposition. Finally, ethylene glycol was added to the solution, resulting in the formation of dialdehyde carboxy cellulose. To obtain tricarboxy cellulose (TCC), a mixture of sodium chlorite and acetic acid (20%) was added to the suspended dialdehyde carboxy cellulose and stirred for 48 h at room temperature. The resulting mixture was washed with deionized water and filtered. The yield of the prepared TCC was determined, and it has been in the range of 79%.

The electric conductivity titration was used to determine the carboxylate content of TCC (Abou-Zeid et al. 2018). The TCC was dispersed in 20 ml of 0.01 M aqueous HCl solution and titrated with 0.01 M sodium hydroxide solution. The carboxylate content (mmol/g) was calculated using Eq. (1):

$$\text{Carboxylate content(mmol/g)} = \left(\left(V_1 - V_0\right) * C_{NaOH}\right)/m \quad (1)$$

where V_1, V_0, and C_{NaOH} are the volumes before titration, after titration, the concentration of NaOH standard solution, and m is the weight of the dried sample.

Preparation of composite membranes

A mixture of BNKT, water suspended TCC, and 4% (based on the dry weight of TCC) polyamide-amine-epichlorohydrin was sonicated for 2 min. The mixture was cast on a Petri dish and dried at 60 °C to give the composite membranes. Different weights of BNKT based on the weight of composite membranes (0, 5, 10, 15, and 20% wt/wt) were used, and

the corresponding films were indexed as C0, C5, C10, C15, and C20, respectively.

Characterization

Fourier transforms infrared spectroscopy (FTIR)

FTIR spectra of the TCC films with/without BNKT were carried out using a Mattson 5000 spectrometer (Unicam, UK) using the KBr technique in absorption mode with a 2 cm^{-1} resolution in the range of 4000–400 cm^{-1}.

Surface morphology and EXD analysis

The surface morphology and the elemental analysis were examined by scanning electron microscope (SEM) on a Quanta FEG-250 coupled with Energy Dispersive X-ray Spectroscopy (TEAM-EDX Model). The images were obtained using an accelerating voltage of 10–15 kV.

Thermogravimetry analysis (TGA)

The thermal stability of the membranes was performed on a heat heavy-difference heat integrated analyzer (Perkin Elmer thermal gravimetric analyzer, TGA7, USA) from room temperature to 800 °C in a nitrogen atmosphere at a heating rate of 20 °C min^{-1}.

Electrical properties

The electrical properties were examined by measuring the real and imaginary parts of the complex impedance (Z′ and Z″) as well as the real and imaginary parts of the complex electrical modulus (M′ and M″) of the samples. The impedance spectroscopy includes the measurement of the real and the imaginary parts of the electrical impedance of the materials as a function of frequency (f) at various parameters of interest, such as composition and temperature (T), etc. The complex impedance is given by Eq. (2);

$$\left(Z^{*} = Z' - j\,Z'' \quad j = \sqrt{(-1)}\right) \tag{2}$$

The real and imaginary parts of the complex impedance (Z′ and Z″) of the composite TCC/BNKT membranes were evaluated by Eqs. (3 and 4), respectively;

$$Z' = \frac{d}{2\pi f A \varepsilon_0} * \left[\frac{\varepsilon''(f)}{(\varepsilon'(f))^2 + (\varepsilon''(f))^2}\right] \tag{3}$$

$$Z'' = \frac{d}{2\pi f A \varepsilon_0} * \left[\frac{\varepsilon'(f)}{(\varepsilon'(f))^2 + (\varepsilon''(f))^2}\right] \tag{4}$$

where d is the thickness of the sample, A is the electrode area, ε_0 is the Permittivity of free space ($8.854*10^{-12}$ F m^{-1}), ε′ (*f*) is the dielectric constant, and ε″(*f*) is the dielectric loss of the samples. The measurements were carried out by a Hioki LCR meter (IM3536) connected to two parallel conducting electrodes with a surface area of 0.29 cm^2. The measurements were recorded over the frequency range from 4 Hz to 8 MHz.

Antimicrobial activity tests

Microorganisms used and conditions

The antibacterial activities of the membranes were tested against six foodborne pathogenic bacteria types, including *Escherichia coli* O157:H7, *Salmonella* Typhimurium, *Acinetobacter baumannii, Listeria monocytogenes, Staphylococcus aureus,* and *Streptococcus faecalis*. The bacteria inoculum was prepared by transferring 100 µl of preserved culture into a tube containing 10 ml Tryptic Soya broth (TSB). The inoculated tubes were stored in the incubator for 24 h at 37 °C. After incubation in the ideal environment, each tube was centrifuged at 5000 rpm for 15 min. The cells-containing pellet was extruded and purified by washing three times with phosphate-buffered saline (PBS) to exclude any undesirable particles. The density of the intended bacteria was Log count 6 CFU/ml (Radwan et al. 2020).

Zone of inhibition (ZOI) measurement

The antibacterial properties of the membranes were investigated by estimating the bacterial inhibition zone using the Kirby–Bauer disc diffusion assay. Aliquots (100 µl) of bacterial suspension were appropriately distributed on top of the surface of the Mueller–Hinton agar (MHA) medium. All tested membranes were cut into small pieces (6 mm) and placed onto the surface of the MHA medium. Afterward, all prepared plates were incubated overnight at

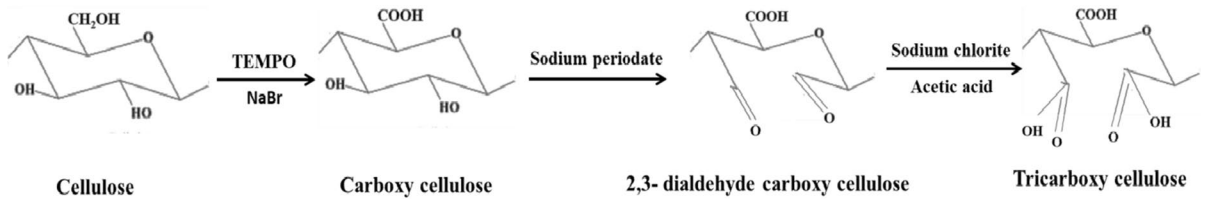

Scheme 1 A plausible mechanism of oxidation of cellulose into tricarboxy cellulose

37 °C. The diameters of the zone of inhibition (ZOI) were estimated in triplicate, measured in millimeters using an electronic caliper (El Nahrawy et al. 2020).

Bacterial growth inhibition test

A fixed-sized sample (5×5 cm^2) of each tested membrane was placed into a tube containing 10 ml of fresh media, which was then inoculated with 100 µl of each microbial suspension for the growth inhibition tests. All tubes were kept at 37°C for various contact times (60, 120, 180, and 240 min) under shaking conditions (250 rpm). An aliquot of the mixture was withdrawn from each sample and tenfold diluted in sterile phosphate-buffered saline PBS. As described above, the dilutions were plated onto agar plates and incubated at 37 °C. Control groups were prepared using an equal volume of PBS. The bacterial growth inhibition tests were performed in triplicate duplicates. The bacterial reduction was calculated using Eq. (5):

$$Log\ reduction = Log\mathrm{CFU}_{control} - Log\mathrm{CFU}_{membranes} \quad (5)$$

Effect of tested membranes on bacterial growth and protein leakage

The growth rate of microorganisms was assessed for all the species. After placing all tubes in a shaker, the optical density (OD) of the samples was measured at 600 nm using a spectrophotometer every 3 h for 24 h at various exposure intervals (0, 3, 6, 9, 12, 15, 18, 21, and 24 h). The Bradford assay was used to estimate the amount of intracellular protein permeability in the targeted bacterial species. After the incubation period, 2 ml aliquots from the tubes were centrifuged at 5000 rpm for 10 min, and the liquid was carefully recovered while discarding the particulates. The effluent from each sample was thoroughly mingled with 0.8 ml of Bradford reagent and incubated in a dark state for 10 min at 37°C. The optical density (OD) was then quantified at 595 nm using bovine serum albumin as a standard reagent (El Nahrawy et al. 2021).

Statistical analysis

The results were carried out in triplicate, and the findings were presented as the mean ± standard deviation (SD).

Results and discussion

The cellulose was oxidized into tricarboxy cellulose (TCC) using a TEMPO oxidizing agent followed by periodate-chlorite oxidation. This oxidation process targeted the primary hydroxyl groups at C6 of the glucose unit, which are considered more reactive than the secondary hydroxyl groups at C2 and C3. In the presence of NaBr and NaClO, the nitroxyl radical acts as a mediator and selectively oxidizes the primary hydroxyl groups. Subsequently, the secondary hydroxyl groups were oxidized using periodate-chlorite (French 2017). This process resulted in the production of tricarboxy cellulose with a carboxylate content of 2.74 mmol/g and a yield of 79% (Scheme 1).

FT-IR analysis

FT-IR spectroscopy is an effective tool with high selectivity and sensitivity for detecting characteristic functional groups in a spectral band, making it useful for analyzing composition changes. The absorption peaks in the FTIR spectrum correspond to the vibration frequency within atom bonds in nanoparticles, as shown in Fig. 1. The FTIR peak intensity directly

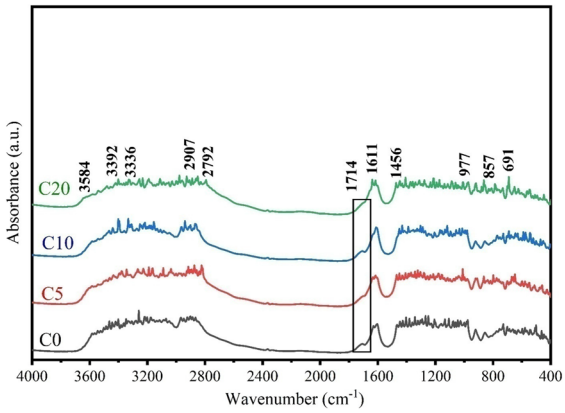

Fig. 1 FTIR of TCC with/without BNKT membranes

indicates the types of components involved, making it an ideal technique for qualitative research.

The spectra of the TCC membranes, with and without BNKT, dried in the air, exhibited peaks in the range 3336–3584 cm^{-1}, attributed to the stretching vibration of OH and H_2O adsorbed on the surface of the membranes. The intensity of these peaks was significantly reduced when BNKT was added, confirming the excellent formation of TCC polymeric/BNKT complex nanocomposites. The most significant difference in the spectra was observed in the bands at ~2792 cm^{-1} and 2907 cm^{-1}, which can be attributed to the C–H stretching of the COOH and/or $–CH_2$ vibrations (Li et al. 2010). The appearance of the weak peak at 1714 cm^{-1} (C=O) might be due to the coordinates between the BNKT nanoparticles and the tricarboxy cellulose, indicating effective loading of BNKT within the TCC matrix (Gao et al. 2013). Another characteristic peak at 1611 cm^{-1} corresponds to the C=O stretching of the carboxyl groups and the bending mode of adsorbed OH in the nanocomposites (Li et al. 2010). These peaks are the characteristic peaks of cellulose (Abou-Zeid et al. 2018). Therefore, the relative change in the intensity of the peaks within the wavenumber range from 691 up to 977 cm^{-1} slightly increases with the increasing amount of BNKT in the TCC, indicating good compatibility between the TCC and the BNKT nanoparticles.

Surface morphology

The morphology of the membrane surface was examined using a scanning electron microscope (SEM) equipped with Energy Dispersive X-ray Spectroscopy (EDX) for element detection (Fig. 2). The SEM images revealed homogeneous structures in the TCC membrane, and the BNKT nanoparticles exhibited a discrete and uniform distribution within the TCC matrix. Increasing the content of BNKT nanoparticles led to a higher percentage of BNKT elements such as Na, Bi, K, and Ti. Additionally, no significant aggregation of BNKT nanoparticles was observed, indicating compatibility between the BNKT nanoparticles and the TCC matrix. Therefore, the casting of a blending solution method is suitable for preparing a uniform composite membrane consisting of TCC with BNKT nanoparticles.

Thermogravimetric analysis (TGA)

TGA is a tool used to evaluate the weight changes of a material as it is exposed to controlled temperature or time in a closed environment (Mansour 2020). In this study, TGA was performed on TCC membranes with and without BNKT at a heating rate of 10 °C/min under an inert N_2 atmosphere to analyze their weight loss and decomposition (Fig. 3). The membranes exhibited similar weight loss behavior due to their similar chemical nature. It can be observed that all the membranes initially experienced a three-stage weight loss. The initial weight loss occurred between 54 and117 °C, corresponding to water evaporation. During this stage, C0, C5, C10, C15, and C20 lost approximately 15, 16, 17, 18, and 19% of their initial weight, respectively. The second degradation stage took place between 187 and 260 °C, corresponding to the decarboxylation and dihydroxylation of cellulose (Abid et al. 2021). The total loss of all membranes is almost the same at this stage. The final decomposition stage began at around 300 °C, leading to complete weight loss of the membranes. The decomposition processes at this stage ended at 339 °C, 337 °C, 334 °C, 328 °C, and 319 °C corresponding to C0, C5, C10, C15, and C20, respectively.

The calculated Broido function (for the 2^{nd} degradation stage or major weight loss process) of the prepared TCC membranes with/without BNKT was calculated and plotted against 1000/T as in Fig. 3b. The thermal kinetic parameters, such as the thermal activation energy (Ea), the Arrhenius constant (A), the activation entropy ΔS, the activation enthalpy ΔH, and the Gibbs free energy change ΔG, are presented

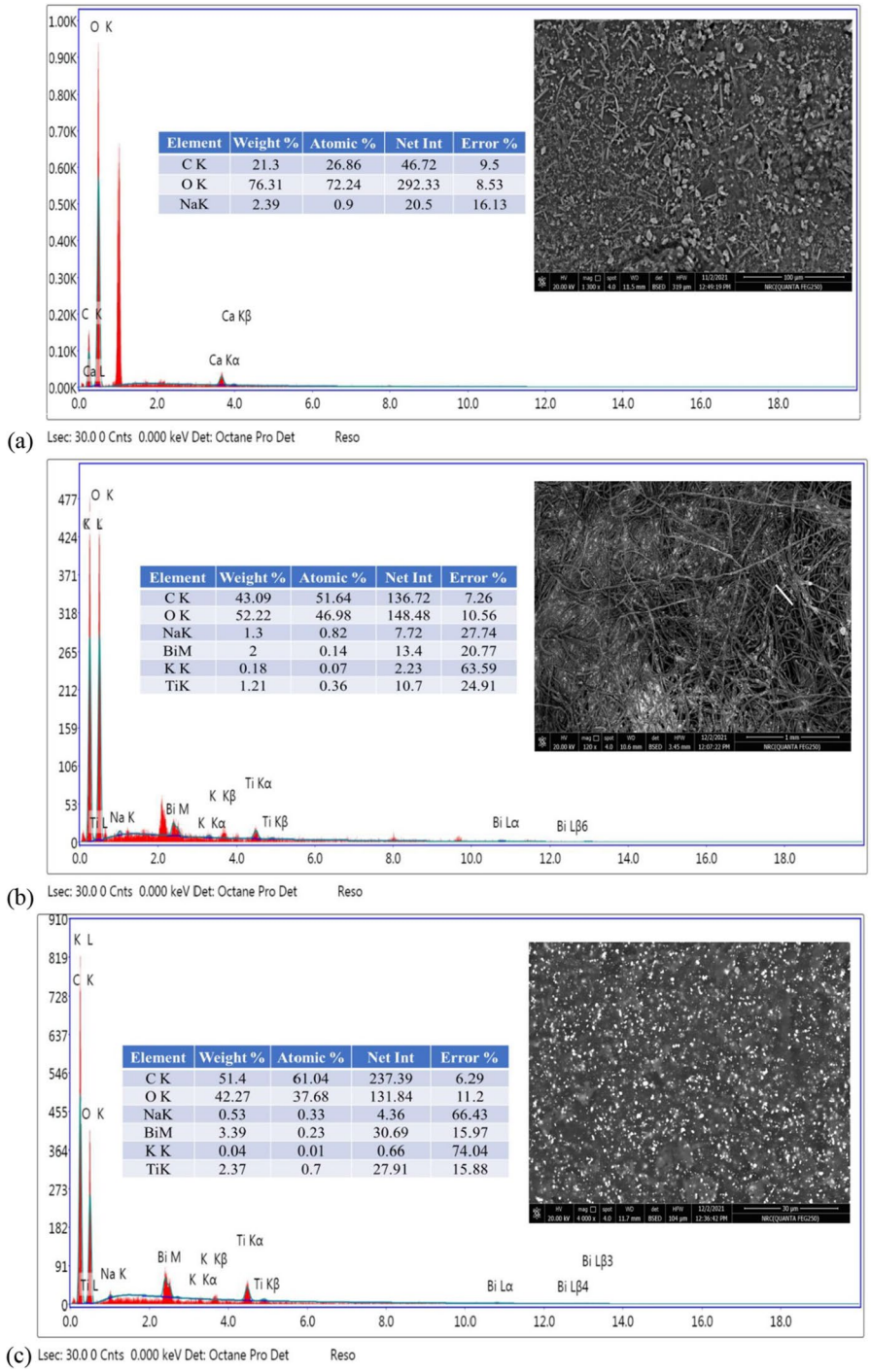

Fig. 2 SEM and EDX analysis of **a**—C0, **b**—C5, and **c**—C15 films

in Table 1. The data in Table 1 displays the decrease of E_a and ΔS and the increase of ΔH and ΔG with the addition of BNKT to TCC. The decline in the activation energy indicates the decline in the thermal stability of the nanocomposites with the addition of BNKT. The exothermic nature of the degradation stage is indicated by the negative ΔH *values*. The + ve sign of ΔS indicates the less-ordered activated state. Finally, the non-spontaneity of the degradation stage is specified by the ΔG + ve sign (Mansour et al. 2019).

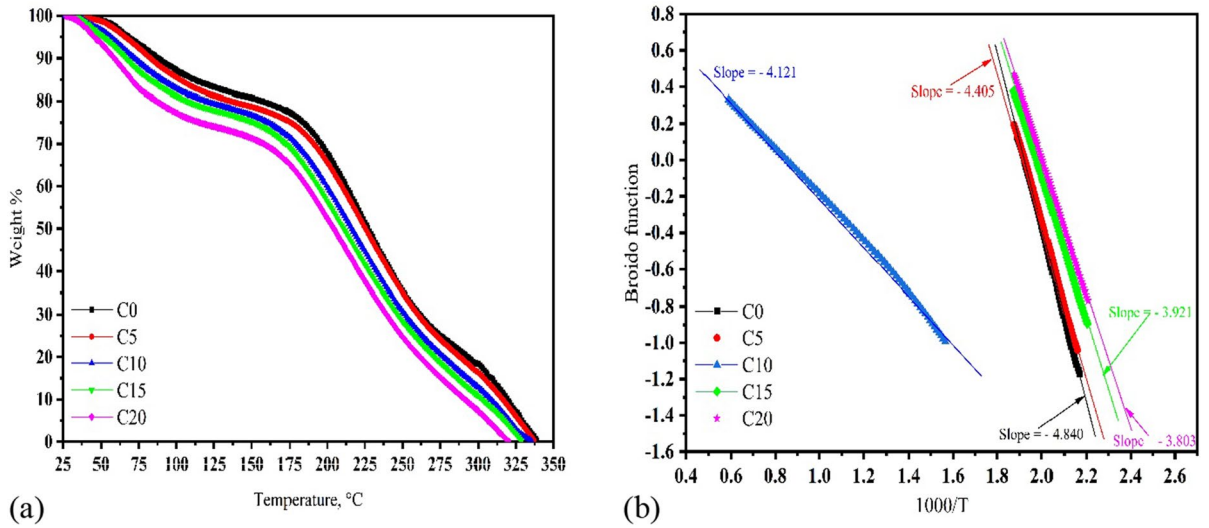

Fig. 3 **a** TGA curves and **b** the corresponding Broido function against 1000/T of TCC membranes with/without BNKT

Table 1 The thermal kinetic parameters, i.e., thermal activation energy (Ea), Arrhenius constant (A), activation entropy ΔS, the activation enthalpy ΔH, and Gibbs free energy change ΔG of TCC films with/without BNKT

Membrane code	Arrhenius constant A (S^{-1})	Activation energy Ea ($Jmol^{-1}$)	Activation entropy ΔS ($Jmol^{-1}$ K^{-1})	The activation enthalpy ΔH ($kJmol^{-1}$)	Gibbs free energy change ΔG ($kJmol^{-1}$)
C0	11,020.36	40.24	171.16	− 3873.23	75,033.08
C5	4777.63	36.62	178.05	− 3844.66	77,706.05
C10	3226.97	34.26	181.22	− 3800.73	78,296.31
C15	2312.99	32.59	183.98	− 3790.75	79,368.22
C20	2028.39	31.61	185.01	− 3764.83	79,307.52

Electrical properties

Impedance (Z′ and Z″)

The real (Z′) and the imaginary (Z″) impedance were evaluated by Eqs. (3 and 4), respectively. The real part of impedance, Z′, was investigated for all the samples as a function of frequency (4 Hz ~ 8 MHz) at different temperatures (20 ~ 160 °C) and presented in Fig. 4. The data in Fig. 4 demonstrates that in the case of C5, the Z′-values decline slowly with increasing frequency up to 10^4 Hz, the impedance in this frequency range is released from the DC resistance. While at $f > 10^4$ Hz, the Z′-values decrease with further increasing frequency up to 10^6 Hz. In this range, the impedance represents the AC resistance. At frequencies higher than 10^7 Hz, the Z′-values remain constant regardless of frequency. Furthermore, as shown in Fig. 4, the Z′ values decrease with increasing temperature in the frequency range of 8 Hz–500 kHz, indicating a thermally activated behavior. For frequencies higher than 500 kHz, the impedance becomes independent of temperature, indicating the liberation of free charge carriers. Similar behavior is observed in the other samples, except for a decrease in impedance values from 35,000 to 6500 Ω and 4500 Ω for C5, C10, and C20, respectively, at the low frequency. This behavior may be attributed to increasing the BNKT content in the samples leading to an increase in the free charge carriers and decreasing the sample's impedance.

Figure 5 depicts the imaginary part of the complex impedance Z″ as a function of frequency (4 Hz–8 MHz) measured at different temperatures

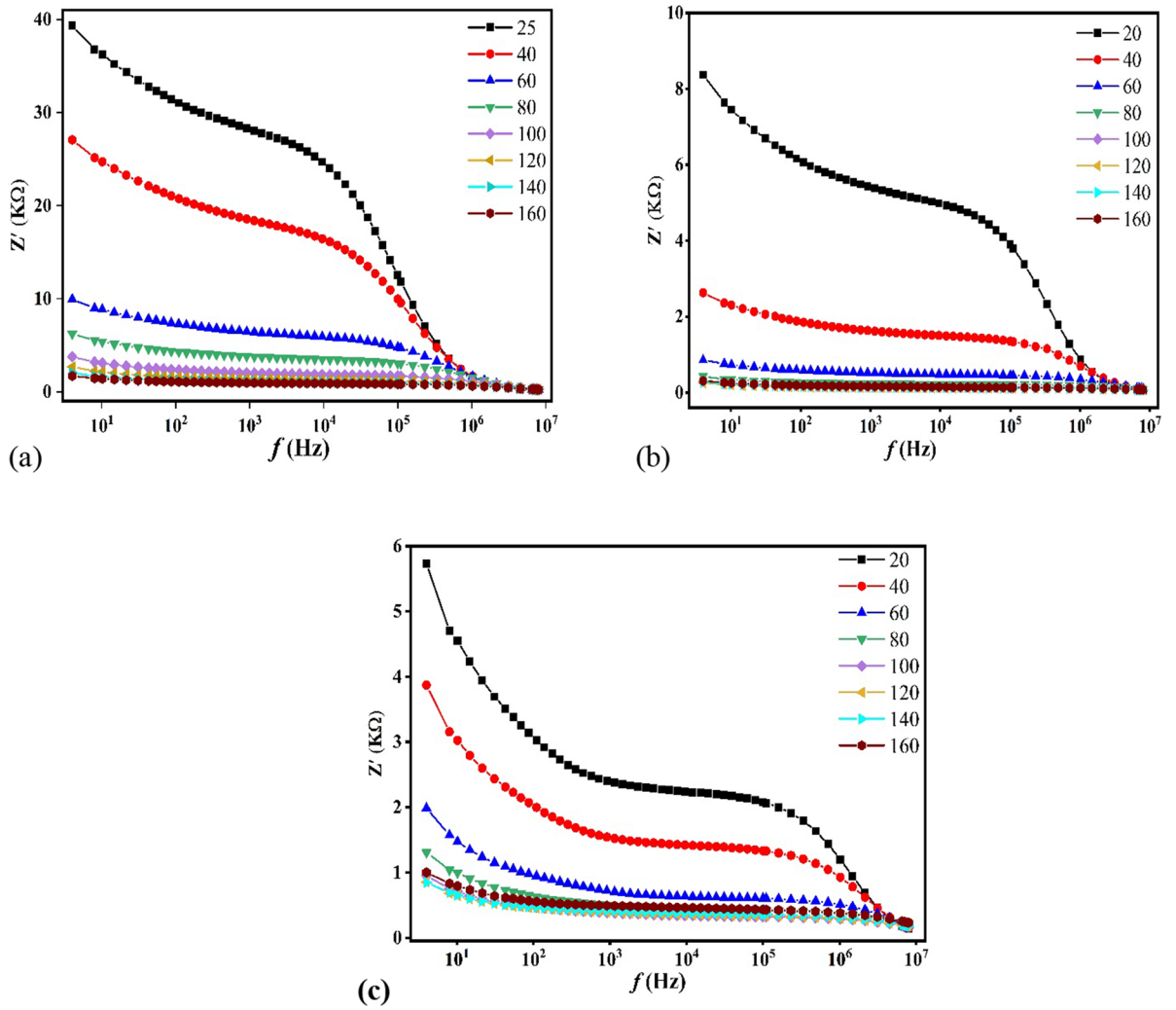

Fig. 4 the real impedance Z′ against frequency at different temperatures for **a**—C5, **b**—C10, and **c**—C20

(20 ~ 160 °C) for TCC/BNKT composite membranes. In terms of the Z″ versus *f* curve, it can be observed that the Z″ values decrease rapidly at low frequencies, which can be attributed to the direct transportation effect of free charge carriers. Furthermore, at the middle-frequency range, the Z″ value increases with increasing frequency until a specific frequency (f_{max}) after it, the Z″ value decreases, this frequency (f_{max}) represents the relaxation frequency that is used to give the relaxation time ($t = 1/2\pi f_{max}$). This peak signifies the transition from long-range hopping at low frequency to the localized motion of the charge carriers at high frequency. Based on Fig. 5, it can be noted that the relaxation peak shifts to higher frequencies with increasing temperature, indicating a decrease in the relaxation time with temperature. This behavior confirms that the samples are thermally activated.

This experimental data confirmed the effect of temperature and frequency on the sample. The same behavior is observed in the TCC/BNKT composite membranes but with a small value of Z″ with increasing the filler (BNKT) content in the membrane. This effect appears due to increasing the filler content leading to an increase in the conducting center in the composite membrane. All the compositions show similar behavior to dielectric materials (Ali et al. 2015).

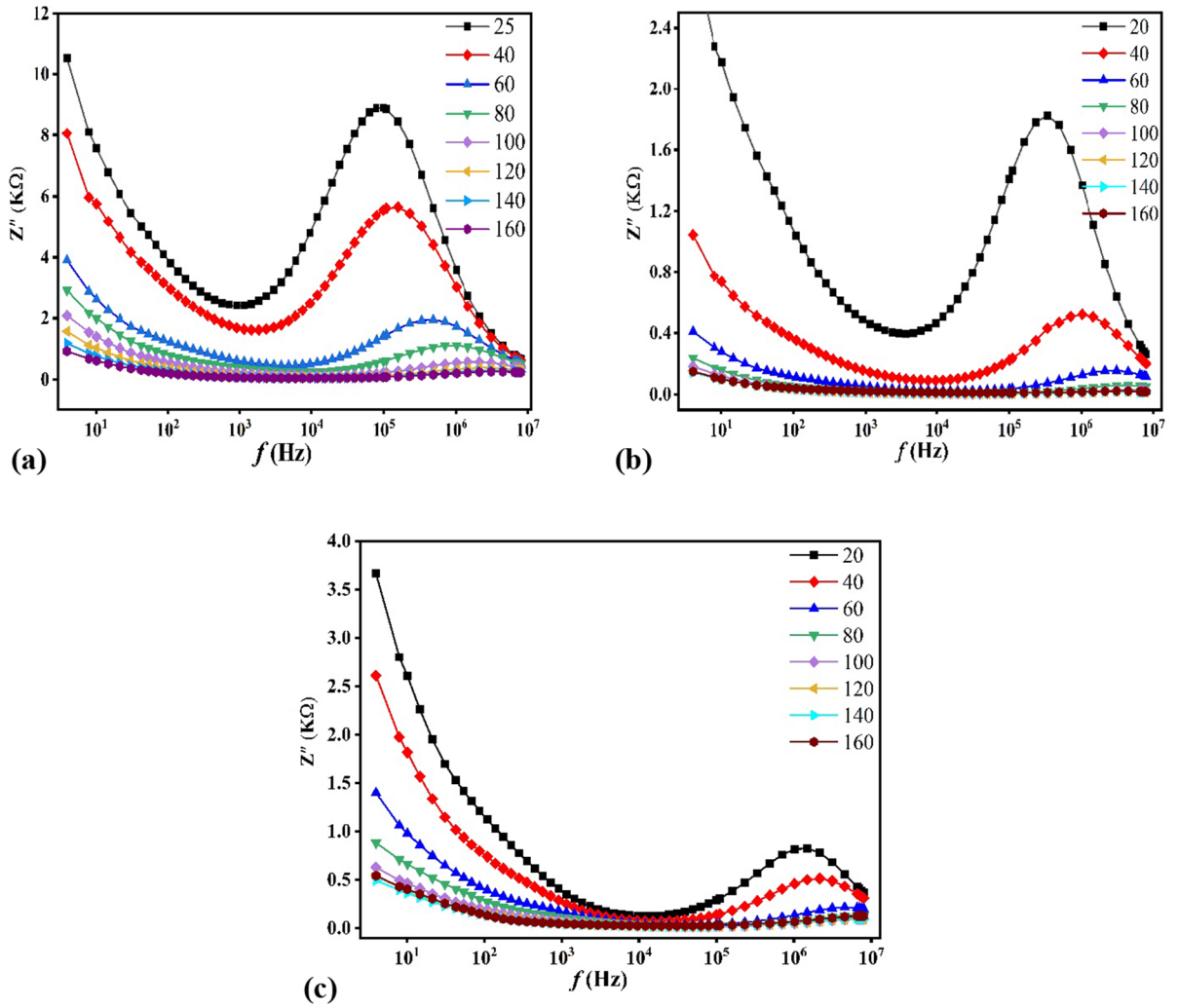

Fig. 5 the real impedance Z″ against frequency at different temperatures for **a**—C5, **b**—C10, and **c**—C20

Figure 6 depicts the real part of the complex impedance, Z′, as a function of temperatures measured at different frequencies for TCC/BNKT composite membranes. Below 60 °C, the Z′ value decreases rapidly with temperature. However, above 60 °C, the Z′ values exhibit a slower decrease with increasing temperature until reaching T = 110 °C. From T = 110 to T = 160 °C, the real part of the impedance remains constant. This behavior confirms that the samples are thermally activated and exhibit semiconductor-like characteristics. In the high-temperature range, the impedance (Z′) appears to be constant and independent of frequency. This behavior can be attributed to the liberation of charge carriers within the samples (Ali et al. 2013a,2013b).

Figure 7 presents the Cole–Cole plot for TCC/BNKT composite membranes at temperatures ranging from 25 to 160 °C. A distinct semi-circle arc is observed for all recorded temperatures, and they exhibit the same behavior. However, as the temperature increases, the radius of the semi-circle arc decreases, indicating a decrease in relaxation time with increasing temperature.

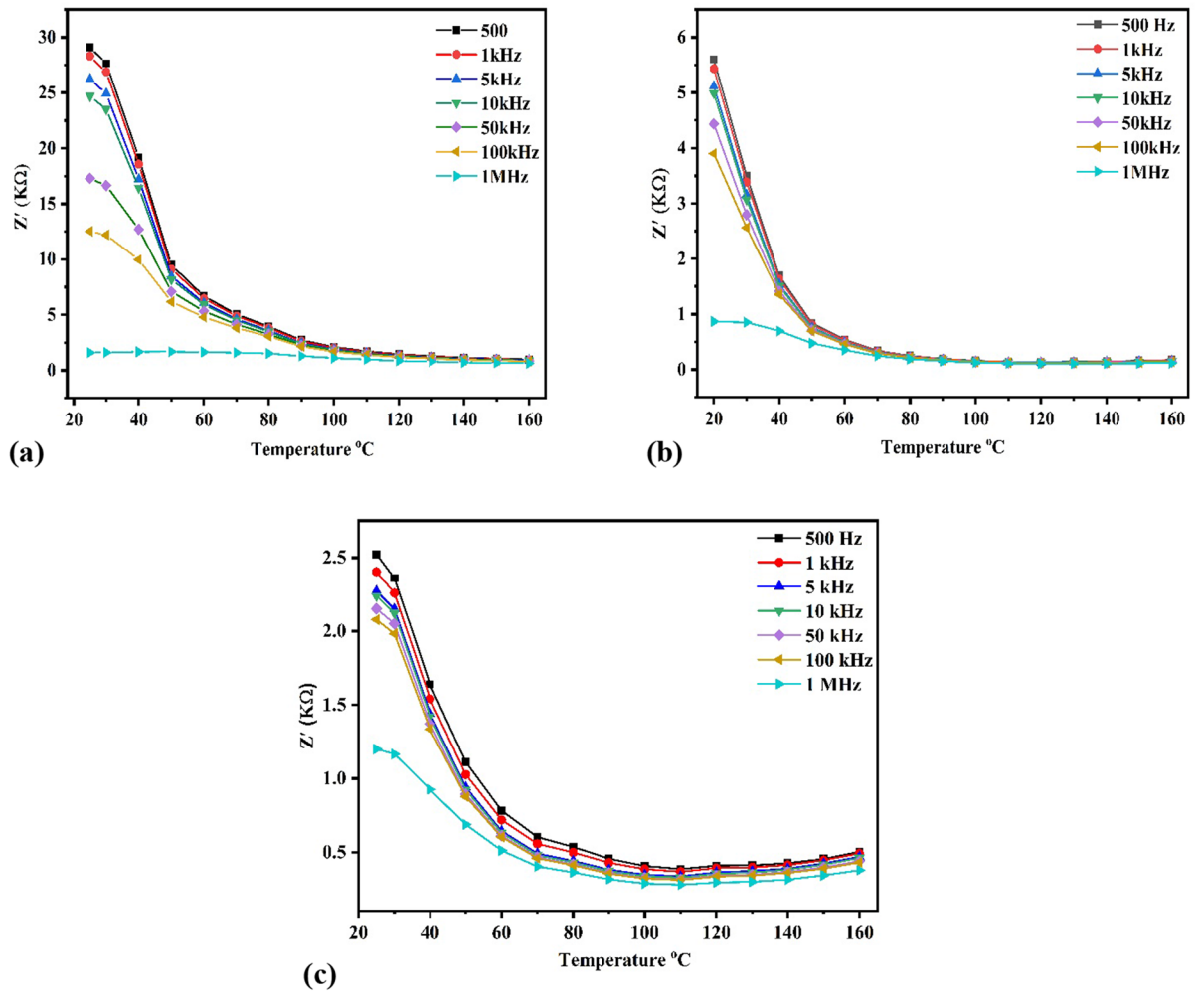

Fig. 6 the real impedance Z′ against temperature at different frequencies for **a**—C5, **b**—C10, and **c**—C20

Electrical modulus analyses

Modulus spectroscopy is a useful technique for analyzing the electrical properties associated with the low capacitance of composites. It can also provide insights into grain boundary conduction mechanisms and electrode polarization (Bhatnagar and Bhatia 1990). Modulus formalism usually describes the relaxation in polycrystalline composites (Rasool et al. 2012). The real and imaginary parts of the complex electrical modulus (M′ and M″) of the TCC/BNKT composite membranes were investigated as a function of frequency (4 Hz ~ 8 MHz) at different temperatures (20 ~ 160 °C) and shown in Figs. 8 and 9. Figure 8 illustrates the variation of the real electrical modulus (M′) with frequency (4 Hz ~ 8 MHz) at various temperatures (20 ~ 160 °C). At higher frequencies, M′ reaches maximum values due to the relaxation phenomena. This behavior is associated with the localized motion and short-range hopping of charge carriers at higher frequencies (Liu et al. 2003; Kaiser 2016). Conversely, at low frequencies (5 Hz to 1000 Hz), M′-values approach zero due to the absence of electrode polarization and the long-range hopping of charge carriers (Ali et al. 2013b).

Figure 9 illustrates the variation of the imaginary part of the electric modulus (M″) with frequency at different temperatures (20 ~ 160 °C). Broad peaks can be observed at high frequencies, which are associated with the relaxation processes

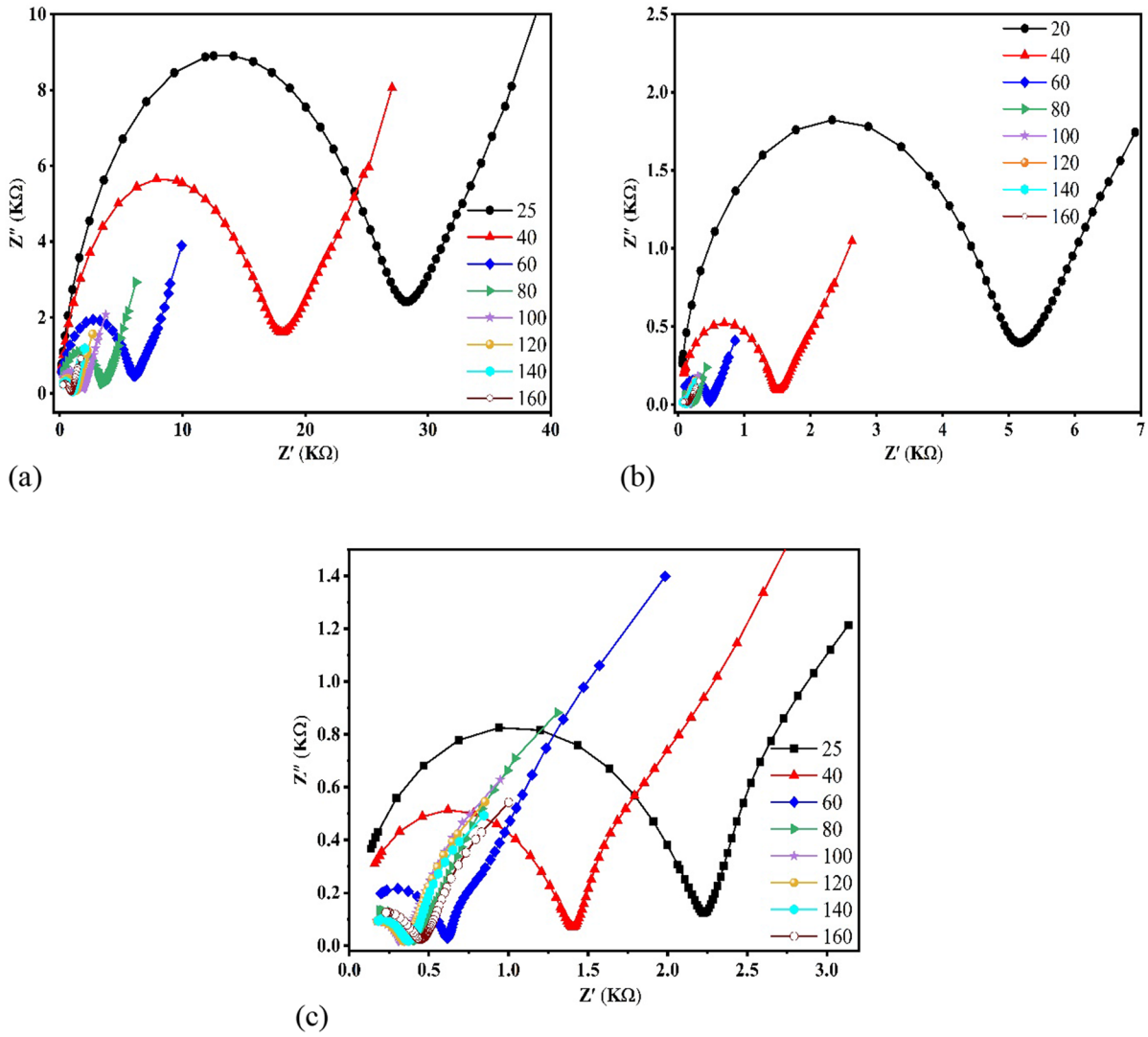

Fig. 7 the Cole–Cole diagram at different temperatures for **a**—C5, **b**—C10, and **c**—C20

occurring in the grains and grain boundaries (Saddeek et al. 2018). The position of these relaxation peaks shifts to higher frequencies as the temperature increases. This behavior indicates that the dielectric relaxation in the material is thermally activated, and it involves the conduction mechanism of charge carriers through hopping, along with the presence of small polarons. These factors play a dominant role in materials that exhibit grain boundary and grain effects (Dhahri 2020).

An antimicrobial assay using the inhibition zone assay

The C20 membrane exhibited the widest zone of inhibition (ZOI) against all six pathogenic organisms studied, with ZOI widths of 20, 22, 19, 15, 17, and 16 mm for *E. coli* O157, *S.* Typhimurium, *A. baumannii, L. monocytogenes, S. aureus,* and *S. faecalis*, respectively (Fig. 10). The narrowest ZOI diameters were observed for C5, for *E. coli* O157, *S.* Typhimurium,

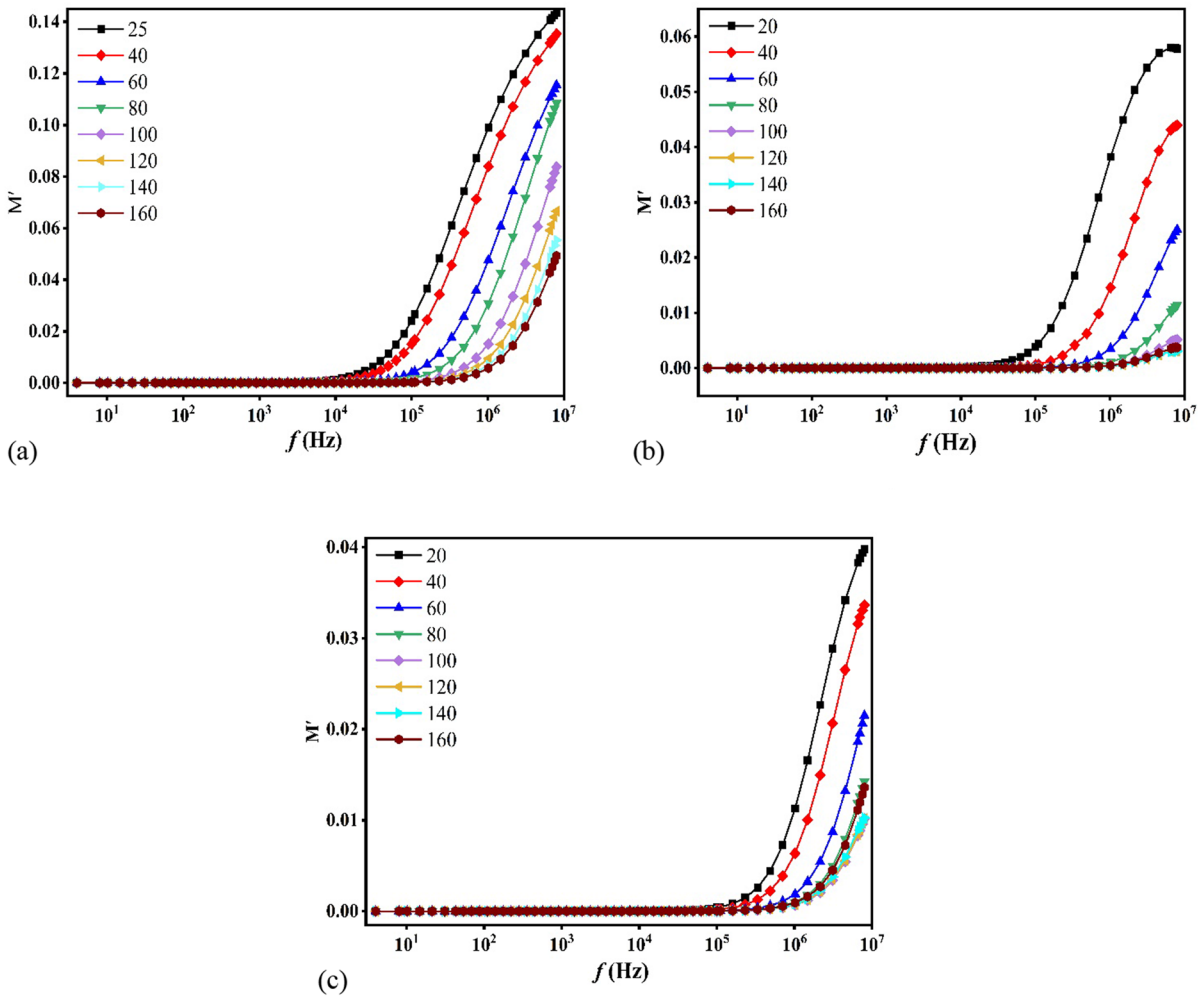

Fig. 8 the real electrical modulus M′ against frequency at different temperatures for **a**—C5, **b**—C10, and **c**—C20

A. baumannii, L. monocytogenes, S. aureus, and *S. faecalis* in the OCF-BNKT membrane, with ZOI diameters of 14, 15, 14, 11, 13, and 12, respectively. On the other hand, the C0 nanomembrane showed no potential antibacterial effect against any of the tested bacteria. Among the studied bacterial species, gram-negative bacteria such as *S.* Typhimurium*, E. coli* O157:H7*,* and *A. baumannii* were found to be the most sensitive.

Bacterial log reduction efficiency

Three membranes (C5, C10, and C20) were selected to be examined for inhibitory effect against tested bacterial pathogens based on ZOI assay. From Fig. 11, it was observed that the control (microorganisms that grew in a usual way without membrane) presented the highest cell populations with 6 log counts. The C20 shows high antimicrobial activity against almost all the bacterial strains tested. First, the C20 can kill both Gram-negative and Gram-positive bacteria very effectively. The results showed a more than 6 log reduction after exposure times 120, 90, 120, 180, 150, and 150 min for *E. coli* O157*, S.* Typhimurium, *A. baumannii, L. monocytogenes, S. aureus,* and *S. faecalis*, respectively. These findings indicate that the nanoparticles could effectively eliminate bacterial cells within a short exposure period. Notably, all Gram-negative species were completely eradicated after 180 min of exposure to the C20

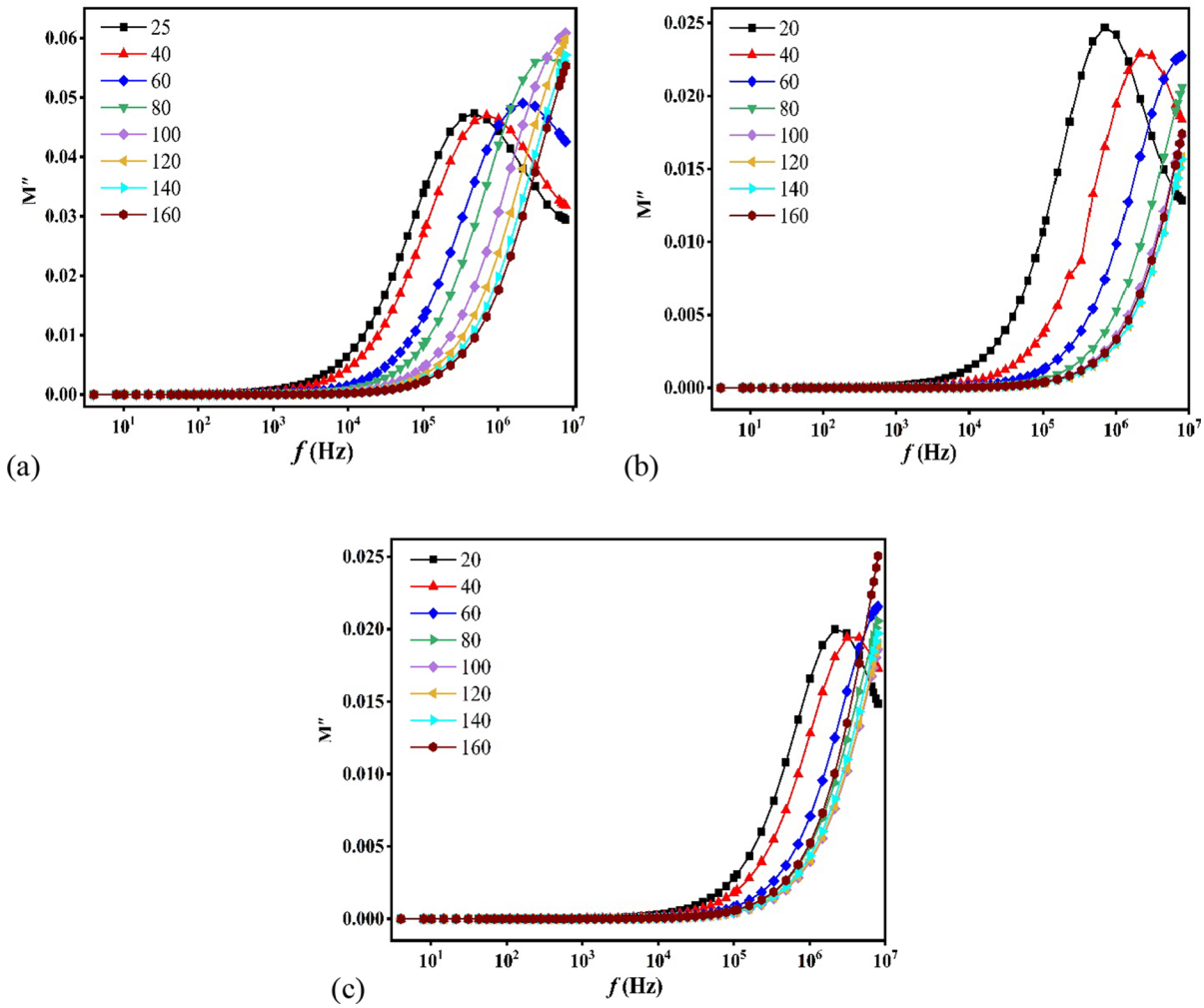

Fig. 9 the imaginary electrical modulus M″ against frequency at different temperatures for **a**—C5, **b**—C10, and **c**—C20

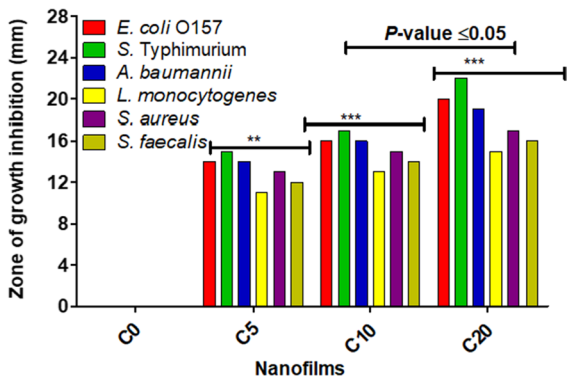

Fig. 10 The antibacterial activity and dimeters of ZOI of four tested nanofilm (C0, C5, C10, and C20) towards standard food borne pathogenic strains

membrane. Therefore, the incorporation of C0 with BNKT nanocomposites enhances the compatibility of the fabricated materials for active packaging applications, providing improved control over food spoilage and the prevention of infections caused by foodborne organisms.

The natural polymer with metal oxide nanocomposite membrane exhibited remarkable biocidal performance against *E. coli*, *P. aeruginosa*, and *S. aureus*. Such fabricated nanocomposite may be applied in food packaging that highly suppresses microbial growth (TRIPATHI et al. 2011). Electrospun TiO_2 nanocomposites have shown significantly higher efficacy against Gram-negative *P. aeruginosa* cells compared to Gram-positive S. aureus

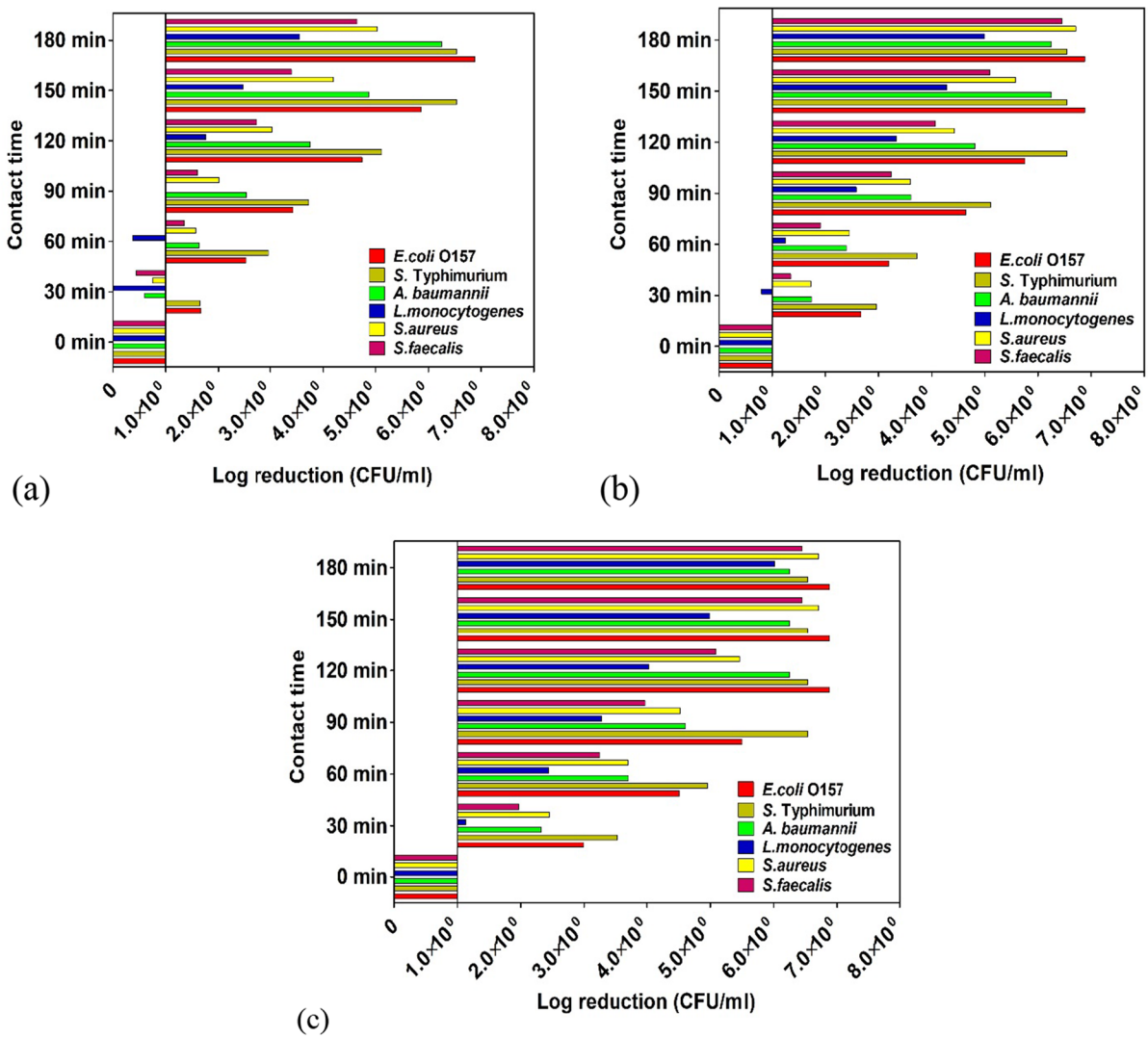

Fig. 11 Log_{10} counts of the survived cells after exposure for 3 h to different dosages of examined engineered nanomaterials, **a**—C5, **b**—C10, and **c**—C20

cells (Ansari et al. 2020). TiO_2-based nanoparticles were employed to develop intelligent polymer-based nanocomposites for salmon filet packaging. This membrane demonstrated synergistic enhancement in antibacterial activity, antioxidant potential, and pH-responsive color-changing indicators (Lan et al. 2021).

Metabolic changes through all tested bacteria

Evaluation of growth curves depending on multiple intervals in the presence of each nanomaterial was used to estimate the readiness of all targeting microbes to proliferate. The results presented in Fig. 12 provide a complete enhancement in the growth curve for each strain without adding membranes (control experiments), emphasizing its growth rate. Conversely, subjecting certain bacteria to each nanomaterial tested using the normalized optical absorbance peak of growth rate substantially declined since these nanomembranes could deadly influence bacterial growth, resulting in a substantial decrease in the slopes of growth curves.

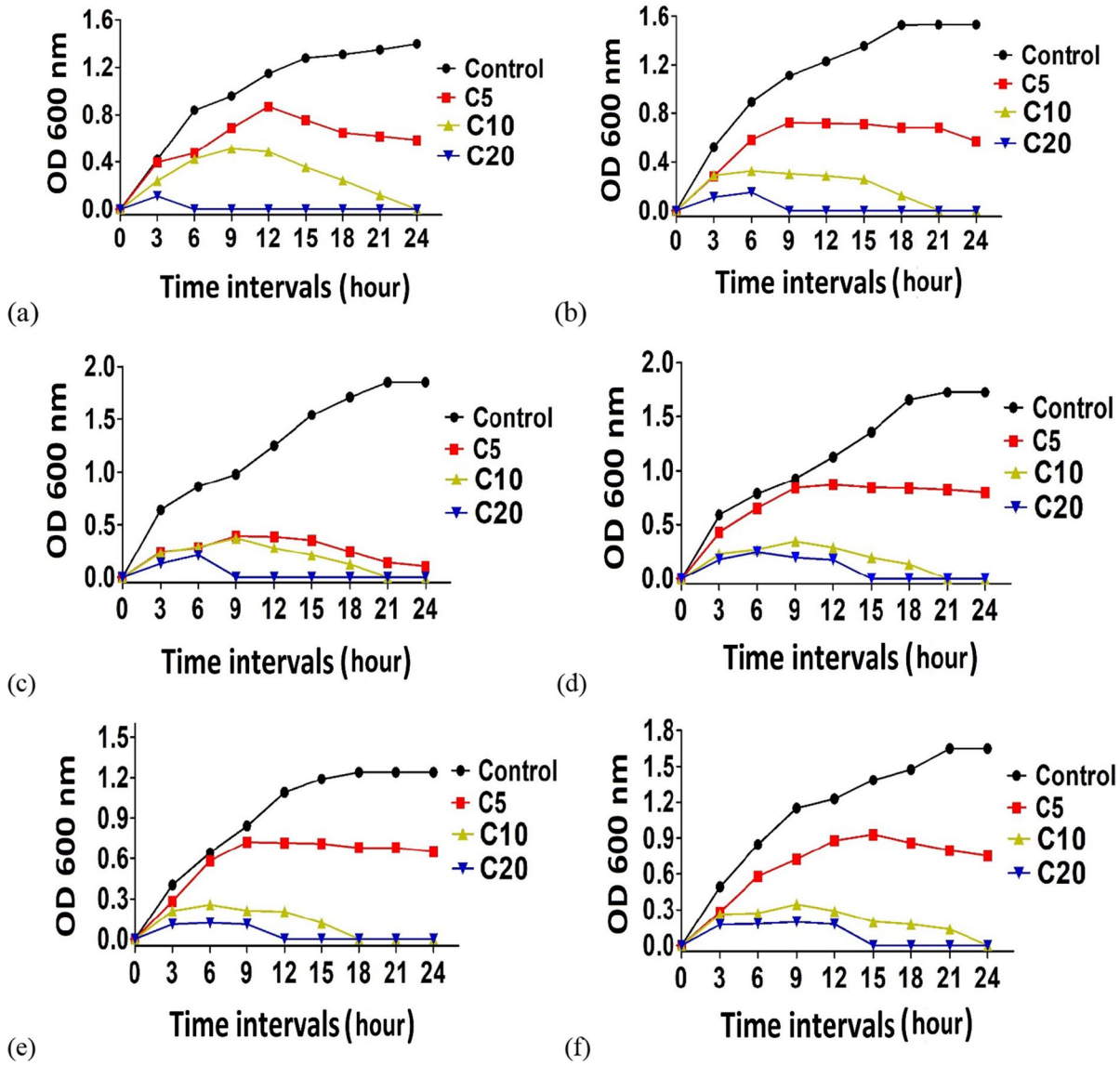

Fig. 12 Growth curves of **a** *E. coli,* **b** *S.* Typhimurium, **c** A. baumannii, **d** *S. aureus,* **e** *S. faecalis, and* **f** *L. monocytogenes*, exposed to three diverse nanomembranes materials (C0, C5, C10, and C20) within 3–24 h

As illustrated in Fig. 13, the gained results revealed that the concentrations of intracellular protein permeability rose sharply in all examined bacteria after treatment to all those nanomembranes compared with the control sample. The proportion of protein spillage from the cells of the controlled experiment, on the other hand, does not fluctuate. The obtained results exhibited the most considerable amount of released protein after exposure to the C20 membrane for all targeted bacterial species. On the other hand, the fewest proportions were recorded for the C20 membrane, signifying the presence of a high concentration of BNKT nanoparticles, which have vigorous antimicrobial properties against a broad spectrum of microorganisms. Furthermore, the elevated proportion of liberated protein from the destroyed bacteria was recorded in all testes bacterial pathogens when exposure duration expanded (3–24 h). The proportion of released protein from *E. coli, S.* Typhimurium, *A. baumannii, S. aureus, S. faecalis,* and *L.*

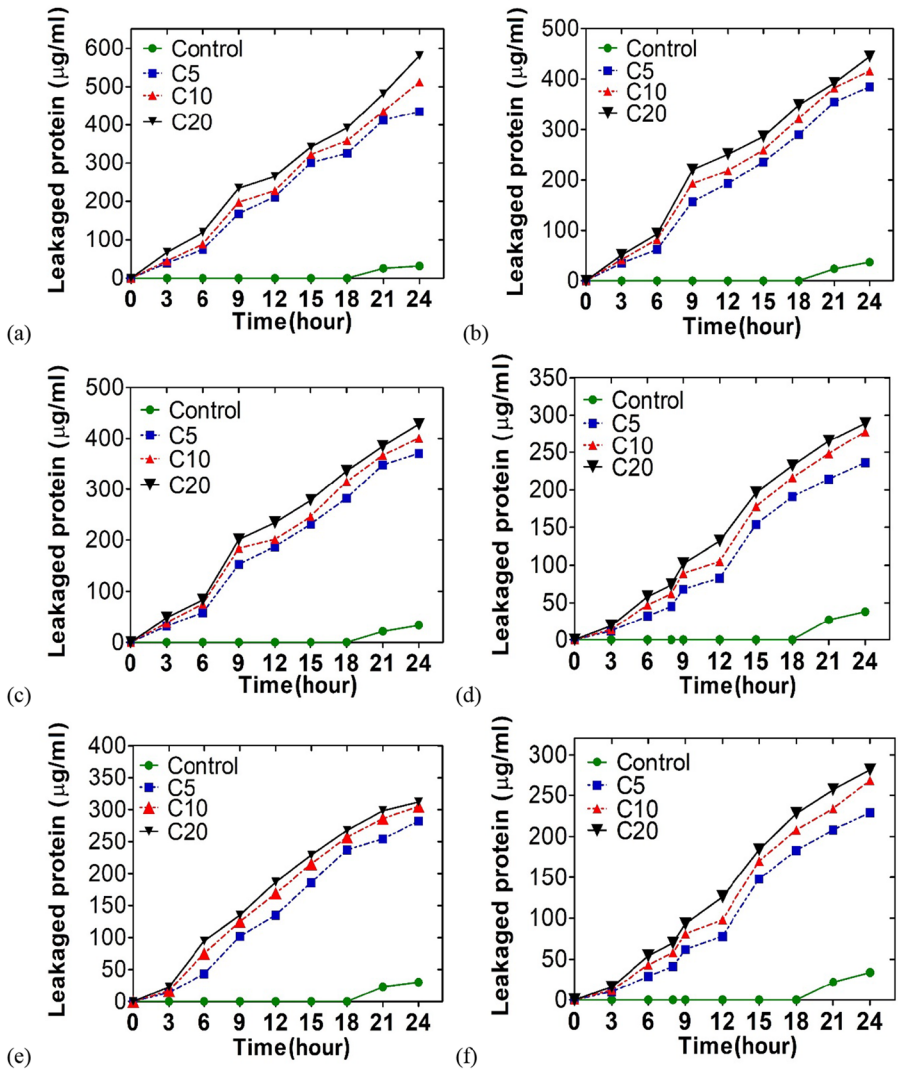

Fig.13 Quantities of released protein from **a** *E. coli,* **b** *S.* Typhimurium, **c** A. baumannii, **d** *S. aureus,* **e** *S. faecalis, and* **f** *L. monocytogenes*, exposed to three diverse nanofilms materials (C0, C5, C10, and C20) within 3–24 h

monocytogenes, were 435, 384, 371,236, 282, and 229 µg/ml, respectively after 24 h of exposure to the C5 membrane. On another side, after being exposed to the C5 nanomembrane, the amounts of released protein were 581, 445, 428, 289, 312, and 281µg/ml, respectively. Meanwhile, the tested C20 nanomembrane was found to be more effective against Gram-negative species than Gram-positive species.

According to the findings, Gram-negative bacterial species membranes leak a greater amount of protein than Gram-positive bacteria membranes; this difference may be due to the shape and thickness of the peptidoglycan layer in the bacterial cell wall. The essential functions of cellular lipid membranes are to protect microbial cells against antimicrobial compounds such as antimicrobial drugs, toxins, and wastes and to destroy metabolites, culminating in less protein permeability in Gram-positive to Gram-negative bacteria (Senthil et al. 2017). Cell membranes and protoplasm account for the majority of microbial species. The cell wall is composed of a predetermined thick layer of peptidoglycan. The cell wall's most prominent purpose is to safeguard microbial cells from hostile external circumstances while modifying them. Bacterial species were classified into two types depending on the makeup of their cell walls: Gram-positive and Gram-negative bacteria. GP species have thick cell walls, approximately 20–80 nm thick attributed to the prevalence of a monolayer of peptidoglycan

polymer (Fu et al. 2005). Gram-negative bacteria's cell walls, on the other hand, have a thin layer of peptidoglycan (7–8 nm) and two cell membranes (outer and cytoplasmic membrane) (Wang et al. 2017). Because some metals have nanoscale shapes, they can easily pierce the cell wall and enter the bacterial cell. Therefore finding them is incredibly challenging to eliminate. The exact mechanism of TiO_2, ZnO, and CuO nanoparticles' antibacterial potential was recently explained (Sirelkhatim et al. 2015; Nguyen et al. 2018; Buazar et al. 2019). The formation of free radicals such as hydroxyl ions, which play an essential role in bactericidal properties, is perhaps the most frequently quoted mechanism (Vallabani et al. 2019). Furthermore, ZnO–NPs interact with cell walls, causing significant damage to the entire bacterial cell, the delivery of antimicrobial ions, particularly Zn ions, and the production of reactive oxygen species (ROS) (Soni et al. 2017). Generally, metal oxide NPs could harm bacteria' cell walls and nuclear DNA by absorption (Suárez et al. 2017).

Conclusion

The loading of BNKT nanoceramics into the TCC matrix modifies the dynamics of the cellulose chains. TGA analysis shows three degradation stages for all membranes, which are attributed to solvent removal, cellulose decarboxylation and dihydroxylation, and the final degradation stages of the membranes. The nanoparticle filler reduces the total impedance of the polymer and thus increases the total conductivity of the polymer. Impedance and modulus studies reveal a Debye-type relaxation phenomenon. Impedance spectroscopy suggests that all samples are thermally activated. The nanoparticle filler increases the wide frequency range of the DC contribution effect. Considering the antibacterial properties of the prepared membrane, the results showed that nanomembrane C20 with 20% BNKT content could be operated as a potential nano-packaging material for biosensors and functional food packaging due to its enhanced conductivity, moisture-sweeping ability, and antimicrobial properties against food-borne pathogenic microorganisms responsible for food spoilage and food outbreaks.

Acknowledgements The authors acknowledge the National Research Center (NRC), Egypt, for financial support of the current work.

Author contributions SK, AMEN designed the study. BAH, AMM, ABAH, AIA, SK, AMEN analyzed the data and wrote the manuscript.

Funding Open access funding provided by The Science, Technology & Innovation Funding Authority (STDF) in cooperation with The Egyptian Knowledge Bank (EKB). Not applicable.

Data and materials availability The data sets used and/or analyzed during the current study are available from the corresponding author on reasonable request.

Declarations

Conflict of interests The authors declare that they have no conflict of interest.

Ethics approval Not applicable.

Consent for publication The authors approve the publication of the manuscript.

References

Abid H, Maqsood Khan S, Iqbal S (2021) A study on optical and thermal properties of natural polymer-based hemicellulose compounds. J Biomater Sci Polym Ed 32:1472–1488. https://doi.org/10.1080/09205063.2021.1925392

Abou-Zeid RE, Dacrory S, Ali KA, Kamel S (2018) Novel method of preparation of tricarboxylic cellulose nanofiber for efficient removal of heavy metal ions from aqueous solution. Int J Biol Macromol 119:207–214. https://doi.org/10.1016/j.ijbiomac.2018.07.127

Ali AI, Ahmed MA, Okasha N, Hammam M, Son JY (2013a) Effect of the La3+ ions substitution on the magnetic properties of spinal Li-Zn-ferrites at low temperature. J Market

Res 2:356–361. https://doi.org/10.1016/J.JMRT.2013.09.001

Ali AI, Ahn CW, Kim YS (2013b) Enhancement of piezoelectric and ferroelectric properties of BaTiO3 ceramics by aluminum doping. Ceram Int 39:6623–6629. https://doi.org/10.1016/j.ceramint.2013.01.099

Ali AI, Hassen A, Khang NC, Kim YS (2015) Ferroelectric, and piezoelectric properties of BaTi 1–x Al x O 3, 0 ≤ x ≤ 0.015. AIP Adv 5:097125. https://doi.org/10.1063/1.4930859

Ansari MA, Albetran HM, Alheshibri MH, Timoumi A, Algarou NA, Akhtar S, Slimani Y, Almessiere MA, Alahmari FS, Baykal A, Low I-M (2020) Synthesis of electrospun TiO_2 nanofibers and characterization of their antibacterial and antibiofilm potential against gram-positive and gram-negative bacteria. Antibiotics 9:572. https://doi.org/10.3390/antibiotics9090572

Bhatnagar VK, Bhatia KL (1990) Frequency dependent electrical transport in bismuth-modified amorphous germanium sulfide semiconductors. J Non Cryst Solids 119:214–231. https://doi.org/10.1016/0022-3093(90)90845-D

Buazar F, Sweidi S, Badri M, Kroushawi F (2019) Biofabrication of highly pure copper oxide nanoparticles using wheat seed extract and their catalytic activity: a mechanistic approach. Green Process Synth 8:691–702. https://doi.org/10.1515/gps-2019-0040

Coseri S, Biliuta G, Zemljič LF, Srndovic JS, Larsson PT, Strnad S, Kreže T, Naderi A, Lindström T (2015) One-shot carboxylation of microcrystalline cellulose in the presence of nitroxyl radicals and sodium periodate. RSC Adv 5:85889–85897. https://doi.org/10.1039/C5RA16183E

Dang Z-M, Yuan J-K, Zha J-W, Zhou T, Li S-T, Hu G-H (2012) Fundamentals, processes and applications of high-permittivity polymer–matrix composites. Prog Mater Sci 57:660–723. https://doi.org/10.1016/j.pmatsci.2011.08.001

Dhahri Kh (2020) Dielectric, ac conductivity and modulus studies of sol–gel $BaZrO_{2.9}$ compound. Phase Transitions 93:802–812. https://doi.org/10.1080/01411594.2020.1789917

El Nahrawy AM, Hemdan BA, Abou Hammad AB, Abia ALK, Bakr AM (2020) Microstructure and antimicrobial properties of bioactive cobalt Co-doped copper aluminosilicate nanocrystallines. SILICON 12:2317–2327. https://doi.org/10.1007/s12633-019-00326-y

El Nahrawy AM, Hemdan BA, Mansour AM, Elzwawy A, AbouHammad AB (2021) Integrated use of nickel cobalt aluminoferrite/Ni2+ nano-crystallites supported with SiO2 for optomagnetic and biomedical applications. Mater Sci Eng, B 274:115491. https://doi.org/10.1016/j.mseb.2021.115491

El Nahrawy AM, Hemdan BA, Mansour AM, Elzwawy A, AbouHammad AB (2022) Structural and opto-magnetic properties of nickel magnesium copper zircon silicate nano-composite for suppress the spread of foodborne pathogenic bacteria. SILICON 14:6645–6660. https://doi.org/10.1007/s12633-021-01295-x

French AD (2017) Glucose, not cellobiose, is the repeating unit of cellulose and why that is important. Cellulose 24:4605–4609. https://doi.org/10.1007/S10570-017-1450-3/FIGURES/3

Fu G, Vary PS, Lin C-T (2005) Anatase TiO_2 nanocomposites for antimicrobial coatings. J Phys Chem B 109:8889–8898. https://doi.org/10.1021/jp0502196

Gao K, Shao Z, Wu X, Wang X, Li J, Zhang Y, Wang W, Wang F (2013) Cellulose nanofibers/reduced graphene oxide flexible transparent conductive paper. Carbohydr Polym 97:243–251. https://doi.org/10.1016/J.CARBPOL.2013.03.067

Goodman SM, Che J, Neri W, Yuan J, Dichiara AB (2022) Water-processable cellulosic nanocomposites as green dielectric films for high-energy storage. Energy Storage Mater 48:497–506. https://doi.org/10.1016/j.ensm.2022.03.047

Hasanin M, Hashem AH, El-Rashedy AA, Kamel S (2021) Synthesis of novel heterocyclic compounds based on dialdehyde cellulose: characterization, antimicrobial, antitumor activity, molecular dynamics simulation and target identification. Cellulose 28:8355–8374. https://doi.org/10.1007/s10570-021-04063-7

Ju J, Chen X, Xie Y, Yu H, Guo Y, Cheng Y, Qian H, Yao W (2019) Application of essential oil as a sustained release preparation in food packaging. Trends Food Sci Technol 92:22–32. https://doi.org/10.1016/j.tifs.2019.08.005

Kaiser M (2016) Magnetic and electric modulus properties of In substituted Mg–Mn–Cu ferrites. Mater Res Bull 73:452–458. https://doi.org/10.1016/j.materresbull.2015.09.015

Kamel S, Khattab TA (2021) Recent advances in cellulose supported metal nanoparticles as green and sustainable catalysis for organic synthesis. Cellulose 28:4545–4574. https://doi.org/10.1007/s10570-021-03839-1

Lal SS, Mhaske ST (2018) AgBr and AgCl nanoparticle doped TEMPO-oxidized microfiber cellulose as a starting material for antimicrobial filter. Carbohydr Polym 191:266–279. https://doi.org/10.1016/j.carbpol.2018.03.011

Lan W, Wang S, Zhang Z, Liang X, Liu X, Zhang J (2021) Development of red apple pomace extract/chitosan-based films reinforced by TiO2 nanoparticles as a multifunctional packaging material. Int J Biol Macromol 168:105–115. https://doi.org/10.1016/j.ijbiomac.2020.12.051

Li SM, Jia N, Zhu JF, Ma MG, Sun RC (2010) Synthesis of cellulose–calcium silicate nanocomposites in ethanol/water mixed solvents and their characterization. Carbohydr Polym 80:270–275. https://doi.org/10.1016/J.CARBPOL.2009.11.024

Liu J, Duan C-G, Yin W-G, Mei WN, Smith RW, Hardy JR (2003) Dielectric permittivity and electric modulus in Bi2Ti4O11. J Chem Phys 119:2812–2819. https://doi.org/10.1063/1.1587685

Mansour AM (2020) Thermal microscopy (TM). Int J Microstruct Mater Prop 15:215–228. https://doi.org/10.1504/IJMMP.2020.110524

Mansour AM, El-Menyawy EM, Mahmoud GM (2019) Structural, optical and galvanomagnetical properties of low cost synthesised nanostructure Cu2S films. Int J Microstruct Mater Prop 14:272–285. https://doi.org/10.1504/IJMMP.2019.099911

Nguyen N-YT, Grelling N, Wetteland CL, Rosario R, Liu H (2018) Antimicrobial activities and mechanisms of

magnesium oxide nanoparticles (nMgO) against pathogenic bacteria, yeasts, and biofilms. Sci Rep 8:16260. https://doi.org/10.1038/s41598-018-34567-5

Palneedi H, Peddigari M, Hwang G-T, Jeong D-Y, Ryu J (2018) High-performance dielectric ceramic films for energy storage capacitors: progress and outlook. Adv Funct Mater 28:1803665. https://doi.org/10.1002/adfm.201803665

Prateek TVK, Gupta RK (2016) Recent progress on ferroelectric polymer-based nanocomposites for high energy density capacitors: synthesis, dielectric properties, and future aspects. Chem Rev 116:4260–4317. https://doi.org/10.1021/acs.chemrev.5b00495

Radwan MAA, Alshubramy MA, Abdel-Motaal M, Hemdan BA, El-Kady DS (2020) Synthesis, molecular docking and antimicrobial activity of new fused pyrimidine and pyridine derivatives. Bioorg Chem 96:103516. https://doi.org/10.1016/j.bioorg.2019.103516

Rasool K, Rafiq MA, Ahmad M, Imran Z, Hasan MM (2012) TiO_2 nanoparticles and silicon nanowires hybrid device: role of interface on electrical, dielectric, and photodetection properties. Appl Phys Lett 101:253104. https://doi.org/10.1063/1.4772068

Saddeek YB, El-Maaref AA, Moustafa MG, El-Okr MM, Showahy AA (2018) A comprehensive study of electrical and optical properties of phosphate oxide-based glasses doped with Er2O3. J Mater Sci: Mater Electron 29:9994–10007. https://doi.org/10.1007/s10854-018-9043-y

Senthil B, Devasena T, Prakash B, Rajasekar A (2017) Non-cytotoxic effect of green synthesized silver nanoparticles and its antibacterial activity. J Photochem Photobiol B 177:1–7. https://doi.org/10.1016/j.jphotobiol.2017.10.010

Sharma R, Jafari SM, Sharma S (2020) Antimicrobial bionanocomposites and their potential applications in food packaging. Food Control 112:107086. https://doi.org/10.1016/j.foodcont.2020.107086

Sirelkhatim A, Mahmud S, Seeni A, Kaus NHM, Ann LC, Bakhori SKM, Hasan H, Mohamad D (2015) Review on zinc oxide nanoparticles: antibacterial activity and toxicity mechanism. Nanomicro Lett 7:219–242. https://doi.org/10.1007/s40820-015-0040-x

Song Y, Wu T, Bao J, Xu M, Yang Q, Zhu L, Shi Z, Hu G-H, Xiong C (2022) Porous cellulose composite aerogel films with super piezoelectric properties for energy harvesting. Carbohydr Polym 288:119407. https://doi.org/10.1016/j.carbpol.2022.119407

Soni D, Gandhi D, Tarale P, Bafana A, Pandey RA, Sivanesan S (2017) Oxidative stress and genotoxicity of zinc oxide nanoparticles to pseudomonas species, human promyelocytic leukemic (HL-60), and blood cells. Biol Trace Elem Res 178:218–227. https://doi.org/10.1007/s12011-016-0921-y

Suárez DF, Monteiro APF, Ferreira DC, Brandão FD, Krambrock K, Modolo LV, Cortés ME, Sinisterra RD (2017) Efficient antibacterial nanosponges based on ZnO nanoparticles and doxycycline. J Photochem Photobiol B 177:85–94. https://doi.org/10.1016/j.jphotobiol.2017.10.018

Takaichi S, Hiraoki R, Inamochi T, Isogai A (2014) One-step preparation of 2,3,6-tricarboxy cellulose. Carbohydr Polym 110:499–504. https://doi.org/10.1016/j.carbpol.2014.03.085

Tripathi S, Mehrotra GK, Dutta PK (2011) Chitosan–silver oxide nanocomposite film: preparation and antimicrobial activity. Bull Mater Sci 34:29–35. https://doi.org/10.1007/s12034-011-0032-5

Vallabani NVS, Sengupta S, Shukla RK, Kumar A (2019) ZnO nanoparticles-associated mitochondrial stress-induced apoptosis and G2/M arrest in HaCaT cells: a mechanistic approach. Mutagenesis 34:265–277. https://doi.org/10.1093/mutage/gez017

Vilela C, Kurek M, Hayouka Z, Röcker B, Yildirim S, Antunes MDC, Nilsen-Nygaard J, Pettersen MK, Freire CSR (2018) A concise guide to active agents for active food packaging. Trends Food Sci Technol 80:212–222. https://doi.org/10.1016/j.tifs.2018.08.006

Wang R, He X, Gao Y, Zhang X, Yao X, Tang B (2017) Antimicrobial property, cytocompatibility and corrosion resistance of Zn-doped ZrO_2/TiO_2 coatings on Ti_6Al_4V implants. Mater Sci Eng, C 75:7–15. https://doi.org/10.1016/j.msec.2017.02.036

Yang J, Xie H, Chen H, Shi Z, Wu T, Yang Q, Xiong C (2018) Cellulose nanofibril/boron nitride nanosheet composites with enhanced energy density and thermal stability by interfibrillar cross-linking through Ca 2+. J Mater Chem A Mater 6:1403–1411. https://doi.org/10.1039/C7TA08188J

Yin Y, Zhang C, Chen J, Yu W, Shi Z, Xiong C, Yang Q (2020) Cellulose/BaTiO3 nanofiber dielectric films with enhanced energy density by interface modification with poly(dopamine). Carbohydr Polym 249:116883. https://doi.org/10.1016/j.carbpol.2020.116883